Available online at www.sciencedirect.com

SciVerse ScienceDirect

Journal of the European Ceramic Society 32 (2012) 2495–2503

www.elsevier.com/locate/jeurceramsoc

Lithium insertion into dense and porous carbon-rich polymer-derived SiOC ceramics

P. Dibandjo [a,1], M. Graczyk-Zajac [b,*], R. Riedel [b], V.S. Pradeep [a], G.D. Soraru [a,**]

[a] *Dipartimento di Ingegneria dei Materiali e Tecnologie Industriali, Università di Trento, Via Mesiano, 77 – 38050 Trento, Italy*

[b] *Institut für Materialwissenschaft, Fachgebiet Disperse Feststoffe, Technische Universität Darmstadt, Petersenstr. 23, 64287 Darmstadt, Germany*

Received 12 October 2011; received in revised form 25 February 2012; accepted 3 March 2012
Available online 31 March 2012

Abstract

Two polymer-derived SiOC ceramics with different amount of carbon were synthesized either as dense or porous SiOC powders. The dense materials were produced up to a maximum temperature of 1400 °C and show a phase separated nanostructure consisting of SiO_2-rich clusters, nanocrystalline SiC and nanocrystalline carbon phase. The corresponding porous materials were obtained by etching the silica phase of the dense SiOC with 20% HF solution. The electrochemical properties of the dense and porous SiOC ceramics in terms of lithium insertion/extraction were studied. Accordingly, the SiOC materials show a first lithium insertion capacity between 380 and 648 mAh g^{-1} followed by significantly lower extraction capacities between 102 and 272 mAh g^{-1}. We consider the free carbon phase present in the ceramic as the major lithium intercalating agent. The porous samples show a stable electrochemical behavior up to 30 cycles while for the dense materials the efficiency drops to almost zero after 10 cycles.

Keywords: Li-ion battery; Anode; SiOC; Polymer-derived ceramic

1. Introduction

The increase in energy density and power density requirements for lithium-ion batteries leads to continuous research for new electrode materials. Currently mostly graphitic materials are used as anode material in lithium ion batteries due to low price and high reversibility despite relatively low capacity (372 mAh g^{-1}), instability during long-time cycling and inadequacy for high power applications.[1,2] In consequence there is still a need of new materials, which could be economically advantageous but would demonstrate higher capacity, longer life time and better high rate capability.

Carbon-containing silicon oxycarbide electrodes for Li-ion batteries have been widely studied by Dahn et al. in the middle of the nineties.[3–7] Nevertheless, there is presently an interest in these ceramic-based materials due to the recently announced commercialization of SiOC ceramic based anodes (by Dow Corning[8]) and the increased availability/lower price of commercial ceramic polymer precursors (PDC's). Recently various SiCN[9–13] and SiOC[14–21] systems of high carbon content have been reported to exhibit a good electrochemical performance in terms of lithium insertion/extraction.

Some of the SiOC compositions show high reversible capacities above 600 mAh g^{-1}.[17,19,20] However, there is still no clear understanding of the type of active sites responsible for such high values of Li storage. Moreover, a basic research on the mechanism of lithium storage in polymer-derived SiOC materials is still required as the final electrochemical properties of the material depend significantly on the chemical composition of the preceramic polymer and pyrolysis temperature. The work of Sanchez and Raj[16] proposes that the unusually high reversible capacity of silicon oxycarbide is due to the presence of silicon sites in which Si atoms share bonds with O and C atoms, the so called mixed silicon oxycarbide units or mixed bonds. On the other hand Fukui et al., working on a microporous silicon oxycarbide glass[18,19] suggested that lithium atoms could also be stored in the glass micropores, besides being stored in the

* Corresponding author. Tel.: +49 6151 16 6343.
** Corresponding author. Tel.: +39 0461 282 454/0461281977.
E-mail addresses: graczyk@materials.tu-darmstadt.de (M. Graczyk-Zajac), soraru@ing.unitn.it (G.D. Soraru).
[1] Present address: Institut de Sciences des Matériaux de Mulhouse (IS2M) LRC, CNRS 7228, France.

0955-2219/$ – see front matter © 2012 Elsevier Ltd. All rights reserved.
doi:10.1016/j.jeurceramsoc.2012.03.010

interstitial spaces or edges of graphene layers formed in situ during the SiOC synthesis procedure.

In the recent years we gained experience in producing porous silicon oxycarbide glasses by etching of dense SiOC materials.[22–25] In particular we have studied how the feature of the porous material correlates with the composition and pyrolysis treatment of the parent dense SiOC glass. Accordingly, we decided to take advantage of our experience and to investigate the electrochemical behavior of dense/porous SiOC glasses with the aim of shedding some light on the role of porosity on the storage capacity of SiOC glasses. We studied two polymer-derived SiOC compositions with different amount of carbon. The porous SiOCs have been obtained by HF etching of the silica phase present in the silicon oxycarbide network, following a reported procedure.[22] In order to promote the formation of porosity through HF etching the SiOC glasses have been pyrolyzed at 1400 °C to increase the phase separation of the silicon oxycarbide network. It is worth saying that the highest Li capacity are usually measured for SiOC glasses pyrolyzed at lower temperature (ca 1000°–1100 °C).[17–21] However, since in this study we are not aiming for high Li insertion capacities but indeed, for comparing the electrochemical behavior of dense and porous materials, we deliberately decided to use the samples treated at high temperatures. The starting preceramic network was obtained by crosslinking a linear polysiloxane containing Si–H groups with different amount of divinylbenzene (DVB).[26] The silicon oxycarbide materials, either in their dense or porous form, have been structurally characterized using X-ray diffraction, Raman and ^{29}Si solid-state NMR spectroscopies, N_2 adsorption and HR-TEM imaging. Finally the Li-intercalation process has been studied by electrochemical methods. Comparison of the electrochemical behavior among the four sets of samples contributes to understand the type of lithium intercalation mechanism in SiOC ceramics.

2. Experimental

2.1. Materials synthesis

All the chemicals were purchased from Sigma–Aldrich and used as received. As siloxane polymer we used a linear polyhydridomethylsiloxane (PHMS, MW = 1900). In a typical preparation the catalyst (platinum divinyltetramethyldisiloxane always 5 ppm relative to the Si compound) and 10, 200 wt% (calculated on the siloxane weight) of divinylbenzene (DVB) were mixed together and then added to the siloxane to prepare the carbon-enriched SiOC preceramic polymers without any addition of solvent. The resulting low-viscous mixture was placed in a test tube which was covered. The cast solution was allowed to stand at room temperature (RT) and complete setting was achieved overnight. After RT setting, the solutions become hard rubbery materials.

All the samples were pyrolyzed using an alumina tubular furnace (Lindberg/Blue) under 150 mL/min of flowing argon. The samples were heated at 5 °C/min and maintained for one hour at a temperature of 1400 °C. The obtained silicon oxycarbide products were milled in an agate mortar and sieved to a particle size smaller than 80 μm. The specimens are denoted as SiOC-*X* where *X* represents the amount of DVB used for the synthesis (10, 200).

Etching of the silicon oxycarbide was performed using a 20 vol% HF solution in H_2O. 0.5 g of the powdered sample was placed in a polypropylene container with the appropriate hydrofluoric acid (HF) solution. The solution was gently stirred at room temperature for 6 h and then filtered and rinsed off with distilled water to remove any residual HF. The sample was then kept inside an oven at 100 °C for one day to dry. Hereafter, the specimen is denoted as SiOC-*X*–HF (10, 200).

2.2. Preparation of electrodes and cells

The electrodes from SiOC-10, SiOC-200, SiOC-10–HF and SiOC-200–HF materials were prepared by mixing the material with 10 wt% polyvinylidene fluoride (PVdF, SOLEF) solution in *N*-methyl-2-pyrrolidone (NMP, BASF). The ratio carbonaceous material/PVdF was 9:1 and was constant for all the samples. NMP was added in order to form homogeneous slurry (about 0.8 g of solvent for 1 g of solution). The slurry was spread on the rough side of copper foil (10 μm, Copper SE-Cu58 (C103), Schlenk Metallfolien GmbH & Co. KG) using hand blade coating technique and dried at 80 °C for 24 h. The active material loading was always between 6 and 8 mg/cm^2. After drying, the circles (electrodes) of 10 mm in diameter were cut. The electrodes were pressed with 40 kN cm^{-2} for 3 min. The weight of electrodes was measured, and then the electrodes were dried under vacuum at 90 °C for 48 h in Buchi oven and transferred directly to the glove box (MBraun Glove Box Systems, H_2O, $O_2 < 1$ ppm) without contact with air.

All the electrochemical measurements were performed in two-electrodes of Swagelok® type cells with SiOC as the working electrode and lithium foil (99.9% purity, 0.75 mm thick, Alfa Asear) as counter/reference electrode. High purity solution of 1 M $LiPF_6$ in ethylene carbonate (EC) and dimethyl carbonate of weight ratio 1:1 (LP30, Merck KGaA) was used as electrolyte. Porous polypropylene membrane (Celgard 2500) was used as separator.

2.3. Characterization techniques

Hermetically closed cells were electrochemically tested by means of galvanostatic and cyclic voltammetry methods using VMP multipotentiostat (BioLogic Science Instruments). For galvanostatic charges the cut-off voltages of 0 and 3 V were applied. A constant voltage float was used when the cell reached the cut-off voltage for slow charging regime (18 mAg^{-1}).

The SiOC-*X* and the SiOC-*X*–HF samples were characterized by X-ray diffraction (XRD) with a synchrotron radiation with a wavelength of 4.562 nm. The Raman spectra were collected using a system inVia Raman microprobe (Renishaw) employing an Ar-ion laser with a wavelength of 514.5 nm.

The ^{29}Si MAS NMR was performed with a MSL300 Bruker with 7 mm probe-head at a spinning rate of 4 kHz. All the ^{29}Si NMR spectra were recorded using one pulse experiments with 90° pulses and 100 s as recycle delays, conditions that allow a

Table 1
Elemental analysis results of the studied silicon oxycarbide samples.

Sample	Element content* (wt%)			xSiC $(1-x)$SiO$_2$ + yC$_{free}$ (mol)			C$_{free}$ (wt%)
	C	O	Si	SiC	SiO$_2$	C$_{free}$	C$_{free}$
SiOC-10	18.6	34.4	42.2	0.29	0.71	0.74	14.1
SiOC-200	44.2	23.4	31.1	0.34	0.66	2.97	40.2
SiOC-10–HF	39.3	17.6	33	0.53	0.47	2.25	35.3
SiOC-200–HF	66	8	19	0.63	0.37	7.47	65.4

* The amount of hydrogen has not been analyzed and is assumed to balance to 100%.

quantitative assessment of the spectra. The experimental spectra were simulated using dmfit modeling software developed, as described in Massiot et al.[26] The analyzed signals arising from the different pyrolyzed samples are labeled as Q (SiO_4), D (SiC_2O_2), T ($SiOC_3$) and X (SiC_4). Spectra were referenced externally to TMS at 0 ppm.

The specific surface area (SSA) and pore size distributions (PSD) of the resulting porous SiOC ceramics were measured by nitrogen gas adsorption at 77 K using an ASAP 2010 (Micromeritics) instrument. SSA was determined from a BET (Brunauer, Emmet and Teller) analysis in the P/P_0 range of 0.05–0.30 using a molecular cross-sectional area for N2 of 0.163 nm^2 and a minimum of 5 data points. The pore size distributions were obtained from the adsorption branch of the isotherm through the BJH (Barret, Joyner and Halenda) analysis.

The HR-TEM images were taken with a TOPCON EM002B transmission electron microscope operated at 200 kV. For the studies, the powder was dispersed in *n*-butanol using an ultrasonic bath and transferred on a carbon-coated grid for measurement.

3. Results

3.1. Structural characterization

3.1.1. Chemical analysis

Chemical analysis results of the as-pyrolyzed SiOCs as well as that of the HF etched samples are reported in Table 1. Increasing the amount of DVB in the starting precursor results into an increase of the C content in the pyrolyzed SiOC from 18.6 up to 44.2 wt%. The HF treatment dissolves SiO_2 with a corresponding decrease of the O content in the HF-treated samples. In Table 1 the composition of the silicon oxycarbide materials is also represented considering the general formula: xSiC $(1-x)$SiO$_2$ + yC$_{free}$.[27] The main difference between the SiOC-10 and the SiOC-200 lies in the amount of C$_{free}$ which ranges from ~14 wt% up ~40 wt%, respectively. On the other hand the relative amounts of SiC and SiO_2 are similar for the two studied compositions: ~0.30 moles of SiC and ~0.70 moles of SiO_2.

3.1.2. Powder XRD and Raman spectroscopy analysis of the studied silicon oxycarbide materials

Before etching, the diffraction pattern presented two broad peaks at $2\theta = 6.4^\circ$ and 10.4° (Fig. 1) attributed to amorphous SiO_2 and β-SiC phase respectively. It is well known that silicon oxycarbibe undergoes, at high temperature, a phase separation with formation of SiO_2-rich nanodomains and nanocrystalline SiC.[28] The two compositions follow this regular evolution.

For both compositions, after HF etching, the XRD pattern show a decrease of the halo of the amorphous silica at $2\theta = 6.4^\circ$, which allows the reflection corresponding to the (0 0 2) plane of graphite at $2\theta = 7.1^\circ$ to emerge from the background. At the same time, reflections corresponding to (1 0 1) planes of graphite at $2\theta = 12.5^\circ$, and the diffraction peaks of β-SiC become more evident (Fig. 1). We also find an increase of the intensity of the peak at $2\theta = 10.4^\circ$. The d value of peak at $2\theta = 7.1^\circ$ can be attributed to the (0 0 2) reflection of graphitic, disordered carbon. Finally, a new peak at $2\theta = 5.4^\circ$ ($d = 4.86$ Å) is assigned to the formation of F-intercalated graphite.[29]

Raman spectroscopy is extensively used for the characterization of graphitic carbon materials.[30] Raman allows to distinguish between low, medium and high structural organization in all types of carbon materials. Fig. 2a and b shows the Raman spectra of the SiOC samples before and after etching. The nature of

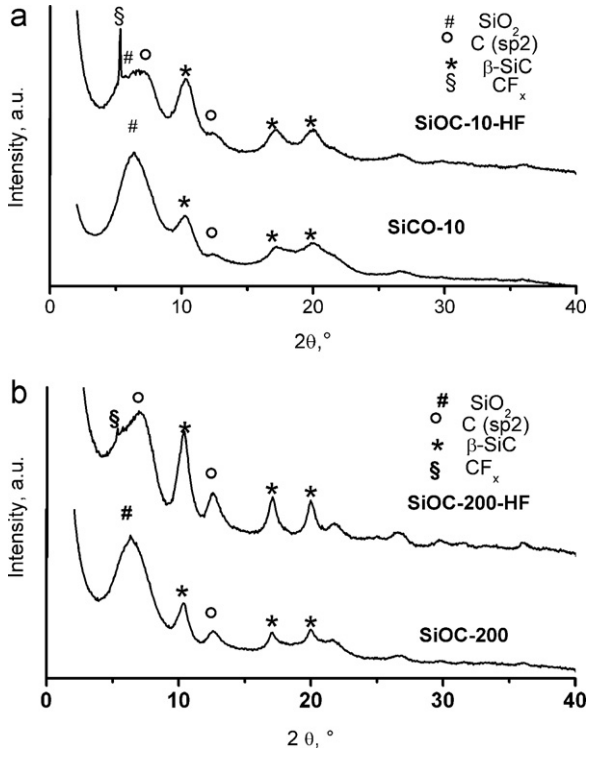

Fig. 1. XRD diffraction patterns of (a) SiOC-10, SiOC-10–HF and (b) SiOC-200, SiOC-200–HF. CFx denotes fluorine-intercalated graphite.

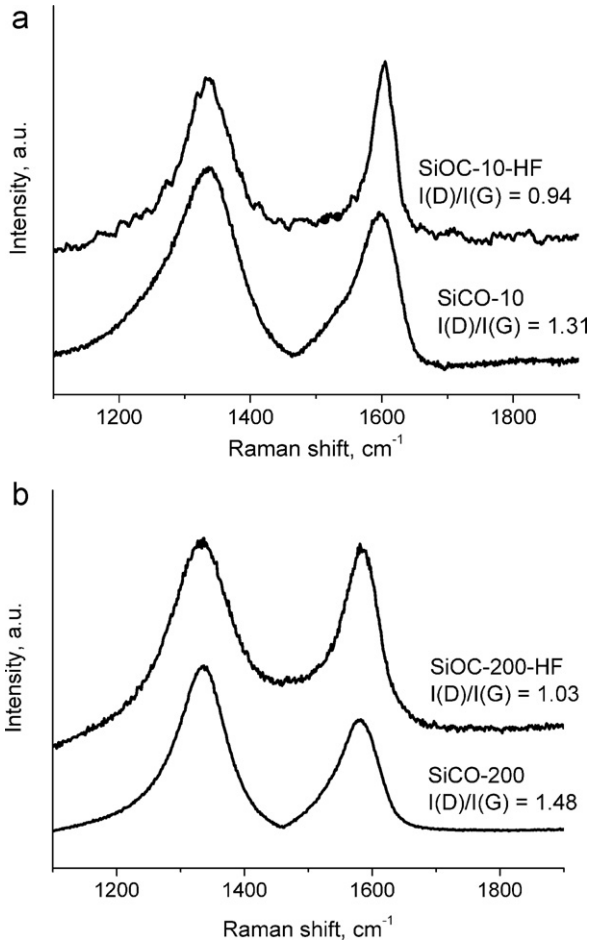

Fig. 2. Raman spectra of (a) SiOC-10, SiOC-10–HF and (b) SiOC-200, SiOC-200–HF samples.

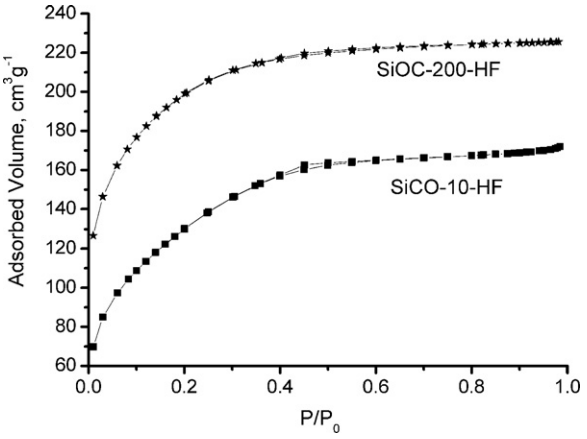

Fig. 3. Nitrogen adsorption/desorption of SiOC-10–HF and SiOC-200–HF.

the Raman spectra is identical in both unetched compositions and is characterized by two bands, with similar intensity, at ~1340 cm^{-1} and ~1600 cm^{-1} which are attributed to the D and G bands of carbon, respectively.[31]

Before etching the intensity ratio of the $I(D)/I(G)$ bands is higher for both, the SiOC-10 and SiOC-200 samples than that of the corresponding etched samples. A high $I(D)/I(G)$ ratio indicates ordering of carbon clusters into nanocrystalline form and has been already discussed elsewhere.[10,31]

After etching, the principal change is a consistent narrowing of the G band, which suggests a higher degree of order of the graphitic carbon structures.[22]

3.1.3. N_2 adsorption analysis

The porous structure of the SiOC samples prepared from PHMS and DVB was characterized by nitrogen sorption method, the obtained results are reported in Table 2. The N_2 adsorption isotherms are characteristic of highly microporous materials with a small hysteresis loop suggesting also the presence of mesopores[32,33] (Fig. 3). The specific surface area (S_{BET}) increases from 460 to 640 m^2/g with the increase of the DVB content. Regarding the mesoporous volume fraction the value did not change with the increase of the DVB, while the microporosity shows a net increase in volume from 0.05 to 0.20 cm^3/g. The pore size distribution does not change with the amount of DVB, having an average value of 2.5 nm. It is important to note that the non etched SiOC-10 and SiOC-200 samples do not present any measurable porosity.

3.1.4. Transmission electron microscopy (TEM) characterization

The overall microstructure of the SiOC samples produced upon pyrolysis at 1400 °C is similar to those of other carbon-rich SiOC materials[34] with fringes of turbostratic carbon, and SiC nanocrystals embedded in an amorphous SiOC matrix. The HR-TEM study does not allow us to clearly differentiate SiOC-10 and SiOC-200 materials as they show a similar microstructure. Accordingly we discuss here the features of both samples based on the HR-TEM images of SiOC-10 composition (Fig. 4a–c). Before and after etching turbostratic carbon features and SiC nanocrystals can be clearly seen (Fig. 4a and b). Moreover, for the HF-etched samples nanopores, which according to the N_2 adsorption analysis have a dimension below

Table 2
SSA, mesopore, and micropore volumes, and pore size (BJH) of carbon based materials.

Samples	SSA (m^2/g) ± 1%	Mesopore volume (cm^3/g)[a] ± 0.01	Micropore volume (cm^3/g)[c] ± 0.01	Average pore size (nm)[b] ± 0.1
SiOC-10–HF	460	0.17	0.05	2.6
SiOC-200–HF	640	0.13	0.20	2.4

[a] Mesopore range = 2–50 nm. Micropore range < 2 nm.
[b] As obtained from the BJH mesopore distribution using the adsorption data of isotherm.
[c] Calculated from the *t*-plot analysis.

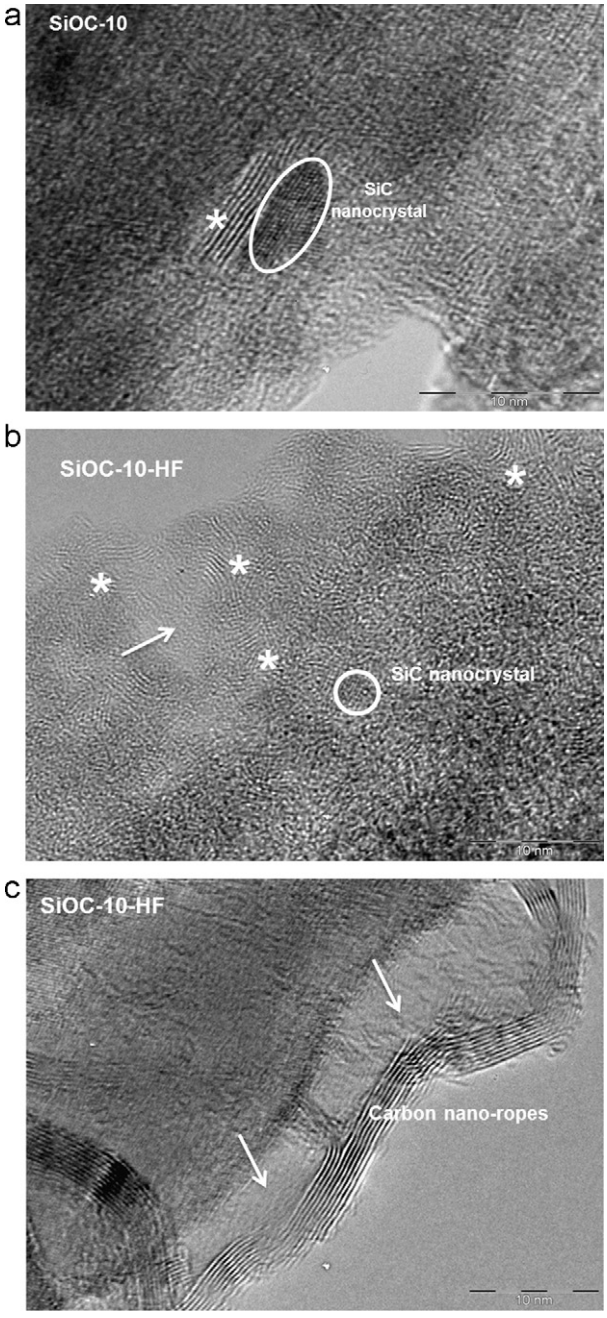

Fig. 4. HR-TEM images of: SiOC-10 (a), and SiOC-10–HF (b and c). Stars indicate turbostratic carbon features while arrows indicate the pores present in the structure.

2.5 nm, can be seen. Interestingly, few large graphitic structures have also been observed (Fig. 4c) consisting of extended graphite nano-ropes formed by several sp_2 carbon planes which reach several tenth of nanometers. Moreover, close to these larger structures, pores extending up to 5–10 nm have also been detected.

In conclusion, the HR-TEM investigation confirms the formation of silicon oxycarbide glasses consisting of a mixture of free carbon in the form of turbostratic carbon and SiC nanocrystals dispersed into a mostly amorphous matrix. In the etched samples predominantly fine pores, in agreement with the N_2 adsorption studies, have been observed with few larger voids (5–10 nm) located close to extended graphite nano-ropes.

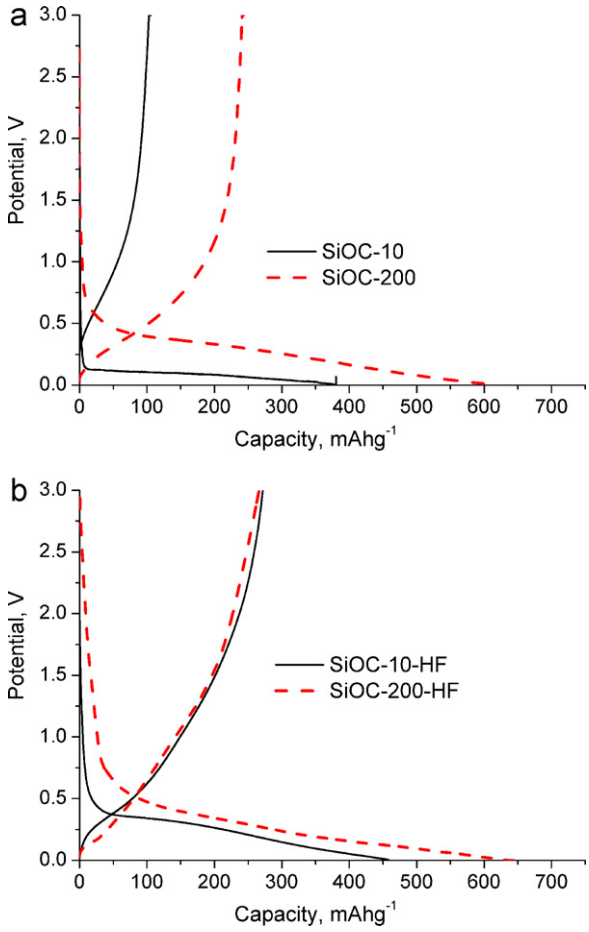

Fig. 5. First lithium intercalation/extraction cycle for SiOC-10 and SiOC-200 electrodes (a), SiOC-10–HF and SiOC-200–HF (b). Charging/discharging rate 18 mA g^{-1}. Solid black line SiOC-10/SiOC-10–HF, dashed red line SiOC-200/SiOC-200–HF. (For interpretation of the references to colour in this figure legend, the reader is referred to the web version of this article.)

3.2. Electrochemical investigation

In Fig. 5 the first lithium insertion/extraction cycles are presented and the electrochemical data are summarized in Table 3. Fig. 5(a) shows the first charge/discharge cycle registered for the SiOC samples before HF etching. A high first charge capacity of 380 and 611 mAh g^{-1} is followed by significantly lower discharge capacities of 102 and 241 mAh g^{-1} for SiOC-10 and SiOC-200, respectively. After etching, the capacities of the SiOC-10–HF and SiOC-200–HF samples (Fig. 5b) are analyzed to 457 and 648 mAh g^{-1} for charging and 272 mAh g^{-1} and 268 mAh g^{-1} for discharging. The lithium insertion into the SiOC-10 sample takes place at the potential < 0.1 V with a long quasi-plateau close to the lithium plating, while the extraction starts at the potential of ~0.5 V. The shape of the intercalation/extraction curves is quite similar for all the other samples besides that of the SiOC-10 material. The lithium intercalation into the SiOC-200 sample starts at about 0.7 V vs. Li. There are also no significant charge losses related to solid electrolyte

Table 3
Capacity values and electrode efficiency of first galvanostatic lithium intercalation/de-intercalation (data from Fig. 5). The efficiency calculated after the 10th cycle is also reported.

Sample	$C_{insertion}$ (mAh g^{-1})	$C_{extraction}$ (mAh g^{-1})	C_{irr} (mAh g^{-1})	η_1 (%)	η_{10} (%)[b]	$C_{discharge}$/g C_{free} (mAh g^{-1})	x value in LiC_x
SiOC-10	380	102	278	27	3	723	3.1
SiOC-200	611	241	370	40	9	600	3.7
SiOC-10–HF	457	272	185	59	35	771	2.9
SiOC-200–HF	648	268	380	42	32	410	5.4
Graphite[a]	434	395	39	91	88	395	5.9

[a] Presented values obtained for graphite are higher than theoretical graphite capacity because for calculations conducting additives were not included to the active mass. In the column before the last one the reversible capacity measured for the first cycle has been normalized for the amount of free carbon calculated from the chemical composition and in the last column the same value has been expressed in terms of LiC_x formula.
[b] Data from Fig. 6.

interphase (SEI) formation and very small hysteresis, i.e. there is a relatively small difference in the potential range between lithium insertion and extraction. Moreover, most of the capacity is recovered up to 1.5 V, which is beneficial regarding possible material application in complete lithium ion batteries. Both samples, SiOC-10 and SiOC-200, do not present any porosity, which results in low amount of SEI formation and hence small capacity losses.

For the etched materials the electrochemical process starts at ~1 V for SiOC-10–HF and at ~2 V for SiOC-200–HF. This electroactivity is related to a pronounced SEI formation due to the higher amount of interface of the porous HF etched samples. Correspondingly, the registered capacity losses related to the SEI formation are much higher for the samples with higher DVB content. Following, a quasi-plateau at 0.3–0.5 V is registered. This plateau and the significant hysteresis (almost 30% of the capacity is recovered over 1.5 V) seem to be typical features of high-capacity SiOC compositions, as already reported by Wilson et al.[5]

The extended charging/discharging behavior of all investigated samples is presented in Fig. 6a–d. For the initial cycles a slow charging/discharging rate of 18 mAg^{-1} was used. After

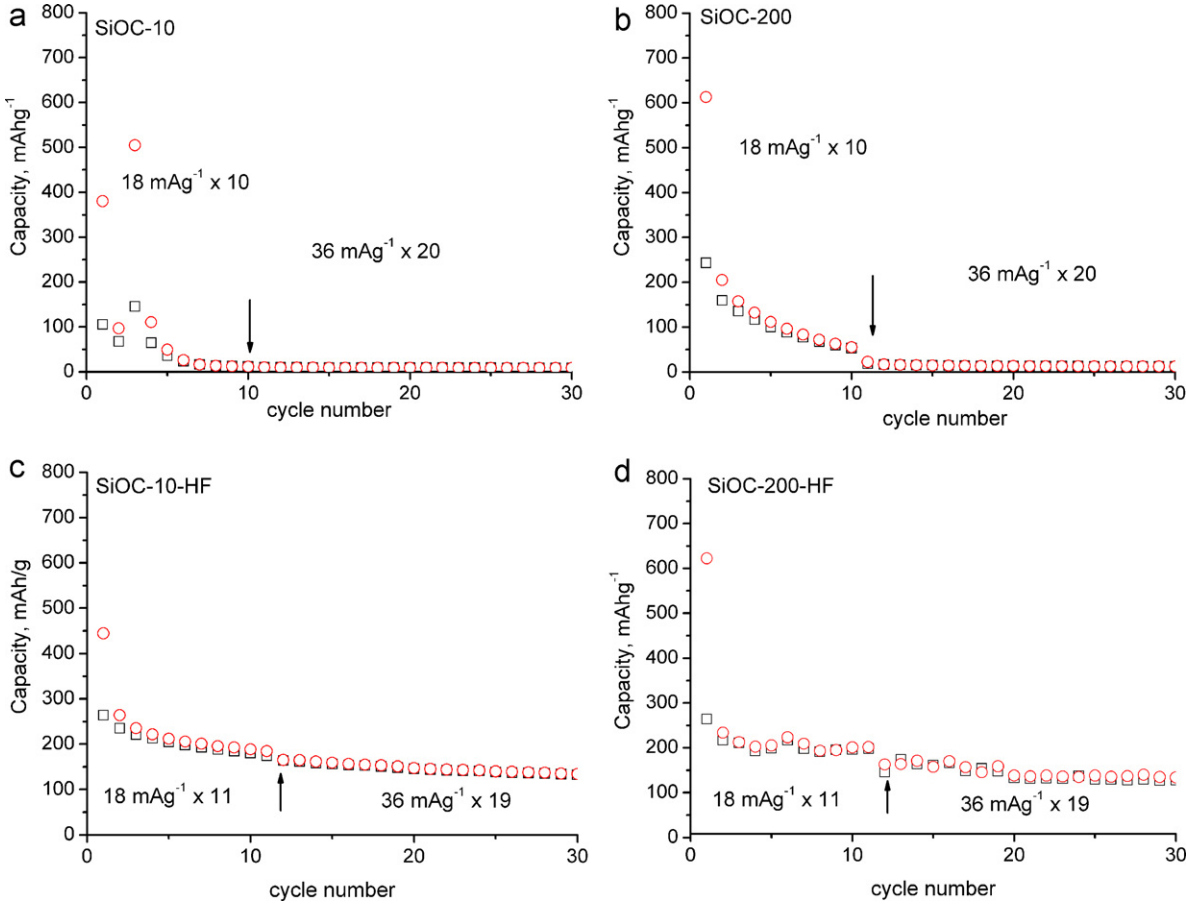

Fig. 6. Cycling behavior (capacity vs cycle number) of samples SiOC-10 (a), SiOC-200 (b), SiOC-10–HF (c) SiOC-200–HF (d) in two-electrode cells. The number of complete charging/discharging cycles and applied current is indicated inside each figure, i.e. 18 mA g^{-1} × 10 means that the cell was ten times charged and discharged with 18 mA/g of active material used. Arrow indicates the cycle with increasing current, charge (squares), discharge (circle).

10 cycles the charging/discharging current was increased up to 36 mAg^{-1}.

The comparison of electrode capacities, the irreversible losses measured during the first cycle ($C_{irr} = C_{charge} - C_{discharge}$) and electrode efficiency η is presented in Table 3. The efficiency, η, is calculated as the ratio of the n-cycle discharge (deintercalation) capacity to the first charge (intercalation) capacity, using the following equation:

$$\eta_n \quad (\%) = \frac{C_{n-\text{discharge}}}{C_{1\text{st-charge}}} \times 100 \tag{1}$$

This value enables an estimation of the quantity of charge captured irreversibly during the n-cycle.

4. Discussion

In spite of the fact that the first charge capacity is higher than that of graphite, the first cycle demonstrates quite high irreversibility for all the studied materials. The first cycle efficiency ranges between 27% and 59%. Irreversibility in these materials is usually accounted for a combination of two processes: (i) formation of poorly reversible structures similar to Li_2O[3] and (ii) to SEI formation.[35] The former should be related to the amount of oxygen present in the SiOC while the latter to the specific surface area. Accordingly, between the two dense materials, the SiOC-10 sample shows a lower efficiency (27%) as compared to that of the SiOC-200 sample (40%) with a significantly lower oxygen content. The high oxygen content in SiOC based materials is considered as a source for high irreversible capacity and significant hysteresis.[36,37] It was found that excessive oxygen works as a trap for lithium ions during the first lithium insertion.[37] On the other hand, the first cycle efficiency of the two porous oxycarbides seems to be more related to their high surface area than to the oxygen content. For these materials the lower efficiency is determined for the SiOC-200–HF sample which has a lower oxygen content but a higher specific surface area and pore volume compared to that of the porous SiOC-10–HF sample.

The first cycle reversible capacities recorded for the SiOC samples ranges from 102 up to 272 mAh g^{-1}. These values are between ca. 27 and 73% of the benchmark for lithium intercalation in graphite (372 mAh g^{-1}) even though the amount of carbon in these materials amounts only 14.1 and 65.4 wt%. In the literature two models have been proposed to explain the lithium storage mechanism in polymer-derived SiOC ceramics. The first one proposed by Raj's group[16] suggests that the mixed Si–C–O tetrahedra are the active sites for Li storage while the second one, proposed in the work of Fukui et al.[19] indicates the interstitial spaces or edges between the graphene layers as the major storing sites. In order to prove these concepts we decided to perform ^{29}Si MAS solid state NMR spectroscopy on the four samples in order to learn more about the structural features of the samples. The results of the solid state NMR studies are presented in Fig. 7 and the corresponding quantitative analysis of the various silicon sites obtained from the simulation of the spectra are reported in Table 4. The spectra of the two as-pyrolyzed samples before HF etching show the presence of two major contributions from Q, SiO_4, ($\delta \approx -108$ ppm) and X, SiC_4,

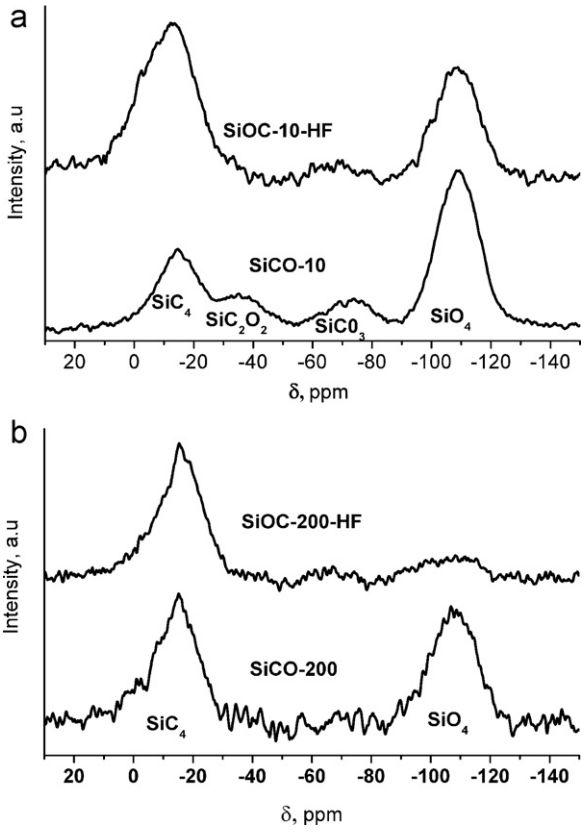

Fig. 7. ^{29}Si MAS NMR spectra of the investigated SiOC samples.

($\delta \approx -16$ ppm) sites. For the low-C content SiOC-10 few mixed T, SiO_3C, ($\delta \approx -72$ ppm) and D, SiO_2C_2, ($\delta \approx -36$ ppm) units are also observed while for the high-C sample, SiOC-200, no mixed silicon oxycarbide units are revealed by this technique. These results agree well with the known high temperature phase separation of the silicon oxycarbide network into SiO_4-rich and SiC_4-rich clusters. Indeed, our samples were pyrolyzed up to 1400 °C for 1 h and, at this temperature; we expect that this type of partitioning of the SiOC matrix has taken place. The NMR spectra of the HF-etched samples show the expected decrease of the SiO_4 units and a corresponding relative increase of the SiC_4 sites. Both samples do not contain mixed Si-O-C units in significant amounts. Based on the NMR data we believe that, in our SiOC samples pyrolyzed at 1400 °C, storage of Li atoms in mixed silicon oxycarbide tetrahedral sites should not play a major role since the samples which contain the highest amount of mixed bonded Si units is the one which shows the smallest first cycle reversible capacity of 102 mAh g^{-1} and the samples

Table 4
Quantitative analysis of the various silicon sites obtained from the simulation of the spectra from Fig. 7.

Samples 1400 °C	X (%) δ (ppm)	D_2 (%) δ (ppm)	T_3 (%) δ (ppm)	Q_4 (%) δ (ppm)
SiOC-10	27 (−14.8)	9 (−35.9)	8 (−72.7)	56 (−108.8)
SiOC-10–HF	61 (−11.5)	–	2 (−69.3)	37 (−108.6)
SiOC-200	48 (−18.4)	–	–	52 (−107.7)
SiOC-200–HF	83 (−16.7)	–	–	17 (−107.2)

which show higher reversible capacities between 241 and 272 mAh g^{-1} contain negligible amounts of mixed tetrahedral SiOC units.

Following the suggestion of Fukui et al.[19] the reversible capacity measured during the first discharge has been ascribed to the free carbon phase and the values have been normalized to the amount of free carbon present in the SiOC ceramics. The results, reported in the last two columns of Table 3 reveal that the carbon phase present in the non-etched silicon oxycarbide matrix can reversibly store almost double the amount of lithium compared to that of commercial graphite, i.e. up to 723 mAh g^{-1} compared to 371 mAh g^{-1}. The same values can be used to get the x value of the LiC_x formula. Accordingly, for commercial carbon anode the x value is 6 (LiC_6) while for silicon oxycarbide glasses x can go down to ≈3. The higher amount of Li atoms that can be reversibly stored in the in situ formed carbon phase in the SiOC matrix could be related to the nano-sized dimensions of the carbon clusters which can store lithium not only in the interstitial spaces of the graphite-like sp^2-carbon structure but also at the edges of the graphene layers. After etching the amount of lithium which can be stored in the free carbon phase remains un-changed for the SiOC-10 composition, with an x value around 3, LiC_3, while for the C-rich sample, SiOC-200, it increases from $x = 3.7$ in the non-etched sample up to 5.4 after etching approaching almost the amount of Li stored by commercial graphite, $x = 6$. The reason why for the low-C SiOC the etching of the silica phase does not change the storage capacity of free carbon while for the high-C sample it does is not clear at the moment. It is known that the HF etching of SiOC not only dissolves silica but can also modify the structure, for example releasing residual stresses[23] or by intercalating F atoms into the graphene layers. These modifications could significantly influence the Li storage and it is likely that the SiOC-200 sample could be more seriously affected by the etching procedure with HF than it is the case for the SiOC-10 ceramic containing much less free carbon.

Another interesting feature of the studied samples emerges from the analysis of the cycling behavior. Etched porous SiOC samples show much better efficiency of about 30% after 10 cycles compared to the dense, un-etched SiOCs. The best first and tenth cycle efficiency is registered for SiOC-10–HF. It should also be noted that cycling has a detrimental effect on the Li-insertion of both dense samples. The charging/discharging capacities vanish and the efficiency drops to almost zero. The good cycling behavior of the porous SiOC compared to the dense material could be due to the different stiffness of the two types of materials. Dense SiOC materials have a high modulus silicon oxycarbide matrix – built up by Si–O and Si–C bonds – in which the carbon phase is embedded.[38] Even if the volume change of the graphite-like clusters during the lithiation/delithiation process is known to be small (about 6%[39]) such a high stiffness network could constrain the free expansion/contraction of the carbon nanocrystals leading to a rapid failure of the storage capacity. On the contrary, in the porous samples the silica phase has been partially removed leading to a less stiff and more compliant structure which improves the cycling stability by increasing tolerance to stress cracking.

5. Conclusions

Dense and porous polymer-derived SiOC samples with different amount of carbon have been processed through pyrolysis at 1400 °C of a linear polysiloxane, PMHS, crosslinked with DVB via hydrosilylation reactions. The dense SiOCs show a phase separated nanostructure consisting of SiO_2-rich clusters, nanocrystalline SiC and nanocrystalline carbon phase. The corresponding porous materials were obtained by etching the dense SiOC with 20% aqueous HF solution. The SiOC materials show a high first charge capacity between 380 and 648 mAh g^{-1} followed by significantly lower discharge capacities between 102 and 272 mAh g^{-1}. The high first cycle irreversibility found for the dense SiOC has been associated to different the oxygen content of the two compositions while for the porous ones the Li charge loss seems more related to the pore volume and the specific surface area of the two samples.

Interestingly, considering that the active phase for Li storage would be the free carbon of the SiOC ceramics, the first cycle reversible capacity, normalized to the amount of this phase, shows that the carbon phase present in the silicon oxycarbide structure can reversibly store almost double the amount of lithium as compared to commercial graphite, i.e. up to 723 mAh g^{-1}. This higher amount of Li atoms that can be stored reversibly in the present carbon phase is related to the nano-sized dimensions of the carbon clusters which can store lithium not only in the interstitial spaces of the sheet-like carbon structure but also at the edges of the graphene layers. Finally the porous samples, being more compliant show a stable electrochemical response up to 30 cycles while for the dense materials the charging/discharging capacities vanish and the efficiency drops to almost zero already after 10 cycles.

Acknowledgments

Research supported by the European Community, through a Marie Curie Research and Training Network "PolyCerNet" (http://www.ing.unitn.it/~soraru//), MRTN-CT-019601. We gratefully acknowledge the financial support by the Deutsche Forschungsgemeinschaft (DFG), Bonn, Germany (SFB 595/A4). Authors thank to Claudia Fasel for elemental analysis measurements.

References

1. Takami N, Satoh A, Hara M, Ohsaki T. Structural and kinetic characterization of lithium intercalation into carbon anodes for secondary lithium batteries. *J Electrochem Soc* 1995;**142**:371–9.
2. Besenhard JO, Winter M, Yang J, Biberacher W. Filming mechanism of lithium–carbon anodes in organic and inorganic electrolytes. *J Power Sources* 1995;**54**:228–31.
3. Xing W, Wilson AM, Eguchi K, Zank G, Dahn JR. Pyrolyzed polysiloxanes for use as anode materials in lithium-ion batteries. *J Electrochem Soc* 1997;**144**:2410–6.
4. Wilson AM, Reimers JN, Fuller EW, Dahn JR. Lithium insertion in pyrolysed siloxane polymers. *Solid State Ionics* 1994;**74**:249–54.
5. Wilson AM, Zank G, Eguchi K, Xing W, Dahn JR. Pyrolysed silicon-containing polymers as high capacity anodes for lithium-ion batteries. *J Power Sources* 1997;**68**:195–200.

6. Dahn JR, Wilson AM, Xing W, Zank GA, inventors; Dow Corning Corp., assignee. Electrodes for lithium ion batteries using polysilanes. United States Patent US 6306541(B1); 23 October 2001.
7. Dahn JR, Eguchi K, Wilson AM, Xing W, Zank GA, inventors; Dow Corning Corp., assignee. Electrodes for lithium ion batteries using polysiloxanes. United States Patent US 5824280(A); 20 October 1998.
8. Kroll P, private communication.
9. Kolb R, Fasel C, Liebau-Kunzmann V, Riedel R. SiCN/C–ceramic composite as anode material for lithium ion batteries. *J Eur Ceram Soc* 2006;**26**:3903–8.
10. Graczyk-Zajac M, Fasel C, Riedel R. Polymer-derived-SiCN ceramic/graphite composite as anode material with enhanced rate capability for lithium ion batteries. *J Power Sources* 2011;**196**: 6412–8.
11. Dahn JR, Wilson AM, Xing W, Zank GA, inventors; Dow Corning Corp., assignee. Electrodes for lithium ion batteries using polysilazanes ceramic with lithium. United States Patent US 5631106(A); 20 May 1997.
12. Graczyk-Zajac M, Mera G, Kaspar J, Riedel R. Electrochemical studies of carbon-rich polymer-derived SiCN ceramics as anode materials for lithium-ion batteries. *J Eur Ceram Soc* 2010;**30**: 3235–43.
13. Kaspar J, Mera G, Nowak A, Graczyk-Zajac M, Riedel R. Electrochemical study of lithium insertion into carbon-rich polymer-derived SiCN ceramics. *Electrochim Acta* 2010;**56**:174–82.
14. Ning LJ, Wu YP, Wang LZ, Fang SB, Holze R. Carbon anode materials from polysiloxanes for lithium ion batteries. *J Solid State Electrochem* 2005;**9**:520–3.
15. Ahn D, Raj R. Thermodynamic measurements pertaining to the hysteretic intercalation of lithium in polymer-derived silicon oxycarbide. *J Power Sources* 2010;**195**:3900–6.
16. Sanchez-Jimenez PE, Raj R. Lithium insertion in polymer-derived silicon oxycarbide ceramics. *J Am Ceram Soc* 2010;**93**:1127–35.
17. Ahn D, Raj R. Cyclic stability and *C*-rate performance of amorphous silicon and carbon based anodes for electrochemical storage of lithium. *J Power Sources* 2011;**196**:2179–86.
18. Fukui H, Ohsuka H, Hino T, Kanamura K. Preparation of microporous Si–O–C composite material and its lithium storage capability. *Chem Lett* 2009;**38**:86–7.
19. Fukui H, Ohsuka H, Hino T, Kanamura K. A Si–O–C composite anode: high capability and proposed mechanism of lithium storage associated with microstructural characteristics. *ACS Appl Mater Interfaces* 2010;**2**:998–1008.
20. Graczyk-Zajac M, Toma L, Fasel C, Riedel R. Carbon-rich SiOC anodes for lithium-ion batteries: Part I. Influence of material UV-pre-treatment on high power properties. Solid States Ionics, http://dx.doi.org/10.1016/j.ssi.2011.12.007, in press.
21. Kaspar J, Graczyk-Zajac M, Riedel R. Carbon-rich SiOC anodes for lithium-ion batteries. Part II. Role of thermal crosslinking, Solid State Ionics, http://dx.doi.org/10.1016/j.ssi.2012.01.026, in press.
22. Peña-Alonso R, Sorarù GD, Raj R. Preparation of ultrathin-walled carbon-based nanoporous structures by etching pseudo-amorphous silicon oxycarbide ceramics. *J Am Ceram Soc* 2006;**89**:2473–80.
23. Pena-Alonso R, Mariotto G, Gervais C, Babonneau F, Soraru GD. New insights on the high temperature nanostructure evolution of SiOC and B-doped SiBOC polymer-derived glasses. *Chem Mater* 2007;**19**: 5694–702.
24. Dibandjo P, Diré S, Babonneau F, Soraru GD. Influence of the polymer architecture on the high temperature behaviour of SiCO glasses: a comparison between linear- and cyclic-derived precursors. *J NonCryst Solids* 2010;**356**:132–40.
25. Soraru GD, Pena-Alonso R, Kleebe HJ. The effect of annealing at 1400 °C on the structural evolution of porous C-rich silicon (boron)oxycarbide glass. *J Eur Ceram Soc* 2012;**32**:1751–7.
26. Massiot D, Fayon F, Capron M, King I, Le Calvé S, Alonso B, et al. Modelling one- and two-dimensional solid-state NMR spectra. *Magn Reson Chem* 2002;**40**:70–6.
27. Soraru GD, D'Andrea G, Campostrini R, Babonneau F, Mariotto G. Structural characterisation and high-temperature behaviour of silicon oxycarbide glasses prepared from sol–gel precursors containing Si–H bonds. *J Am Ceram Soc* 1995;**78**:379–87.
28. Bréquel H, Parmentier J, Walter S, Badheka R, Trimmel G, Masse S, et al. Systematic structural characterization of the high-temperature behavior of nearly stoichiometric silicon oxycarbide glasses. *Chem Mater* 2004;**16**:2585–98.
29. Hamwi A. Fluorine reactivity with graphite and fullerenes. Fluoride derivatives and some practical electrochemical applications. *J Phys Chem Solids* 1996;**57**:677–88.
30. Eklund PC, Holden JM, Jishi RA. Vibrational modes of carbon nanotubes; spectroscopy and theory. *Carbon* 1999;**33**:959–72.
31. Tuinstra F, Koenig JL. Raman spectrum of graphite. *J Chem Phys* 1970;**53**:1126–30.
32. Rouquerol J, Avnir D, Fairbridge CW, Everett DH, Haynes JH, Pernicone N, et al. Recommendations for the characterization of porous solids. *Pure Appl Chem* 1994;**66**:1739–58.
33. Sing KSW, Everett DH, Haynes JH, Hall RAW, Moscou L, Rouquerol J, et al. Reporting physisorption data for gas/solid systems with special reference to the determination of surface area and porosity. *Pure Appl Chem* 1985;**57**:603–19.
34. Kleebe HJ, Blum YD. SiOC ceramic with excess free carbon. *J Eur Ceram Soc* 2008;**28**:1037–42.
[35]. Winter M, Moeller K-C, Besenhard JO. Carbonaceous and graphitic anodes. In: Nazri FA, Pistoia G, Nazri G-A, Pistoia G, editors. *Lithium batteries. Science and technology*. Kluwer Academic Publisher; 2004. p. 144–80.
36. Wilson AM, Xing W, Zank G, Yates B, Dahn JR. Pyrolysed pitch-polysilane blends for use as anode materials in lithium ion batteries II: the effect of oxygen. *Solid State Ionics* 1997;**100**:259–66.
37. Larcher D, Mudalige C, George AE, Porter V, Gharghouri M, Dahn JR. Si-containing disordered carbons prepared by pyrolysis of pitch/polysilane blends: effect of oxygen and sulfur. *Solid State Ionics* 1999;**122**:71–83.
38. Sorarù GD, Dallapiccola E, D'Andrea G. Mechanical characterization of sol–gel-derived silicon oxycarbide glasses. *J Am Ceram Soc* 1996;**79**:2074–80.
39. Winter M, Besenhard JO. Electrochemical lithiation of tin and tin-based intermetallics and composites. *Electrochim Acta* 1999;**45**:31.